Cogging Torque Suppression for IPMSM Based on Flux Harmonic Configuration

Litao Dai, *Member, IEEE*, Jian Gao, Shuangxia Niu, *Senior Member, IEEE,* Kun Liu, Shoudao Huang, *Senior Member, IEEE*, and W. L. Chan, *Senior Member, IEEE*

***Abstract*—Cogging torque, an undesirable pulsating torque inherent in permanent magnet (PM) machines, is caused by the harmonic interaction between rotor flux and airgap reluctance. Therefore, reducing cogging torque can be achieved by minimizing the undesired harmonics of the rotor flux. However, completely eliminating flux harmonics to achieve a purely sinusoidal flux is challenging, especially for interior-PM machines. As an alternative approach, this paper presents a new design method for suppressing cogging torque by configuring the specific odd-order harmonics of the rotor flux. Specifically, the desired flux harmonics is configured by artificially shaping the rotor profile to modulate even-order rotor reluctance harmonics. The proposed method requires minimal parametric design and has minimal impact on other critical performance aspects of the machine due to the limited changes made to its structure. This paper provides a comprehensive implementation pathway for the proposed method, supported by detailed analysis through multiple case studies. Furthermore, the effectiveness of the proposed method is validated through extensive simulations and experiments, confirming its capability to suppress cogging torque and overall torque ripple.**

***Index Terms*—Permanent magnet machines, torque, design methodology.**

I. Introduction

COGGING torque is an inherent and undesirable pulsating torque in permanent magnet (PM) machines, which is generated by the interaction between the rotating flux and the non-uniform air-gap reluctance [1]. It can significantly impact the starting and low-torque performance of PM machines, resulting in torque fluctuations and impairing motor control performance. Therefore, there is a strong motivation to mitigate cogging torque in motor applications [2].

Extensive research has been conducted on cogging torque reduction, leading to the development of diverse and effective methods. These methods primarily involve structural design [3]-[20], with some also incorporating motor control technique [21]. Structural design approaches can be further classified into stator-based design [3]-[8], rotor-based design [9]-[17], the exploration of various pole-slot combinations [18], and design optimization for multiple structural parameters [19]-[20].

Firstly, stator-based design methods have been employed to reduce cogging torque by optimizing the stator shape. The influence of key parameters such as slot opening, tooth profile, and tooth-tip shape on cogging torque has been thoroughly studied [3], [4]. Moreover, unconventional stator structures, including dummy slots [5], slot-opening shifts [6], skewed slots [7], and asymmetric assembly [8], have been proposed to effectively mitigate cogging torque and have shown promising results.

Secondly, rotor-based designs have focused on configuring the rotor magnetomotive force (MMF) harmonics to minimize cogging torque. Researchers have explored the use of different PM shapes [9]-[11] and asymmetric magnetic pole designs, such as asymmetric interior PM (IPM) [12], [13] and surface-mounted PM structures [14], [15]. Additionally, techniques like skewing and segmental shifting of PMs have been studied [7], [16], [17] for their effectiveness in reducing cogging torque.

Moreover, the combination of the number of poles and slots [18], as well as the global optimization of multiple structural parameters [19], [20], have been recognized as crucial factors influencing cogging torque and have been investigated accordingly.

Furthermore, motor control methods have been utilized to suppress cogging torque by injecting current harmonics into the armature windings. This generates a pulsating torque in the opposite direction of the cogging torque, effectively canceling it out [21].

However, the classical methods mentioned above tend to introduce undesirable effects, such as: 1) skewed slots, skewed poles increase the manufacturing and assembly costs; 2) dummy slots reduce the airgap flux density and torque density; 3) asymmetric poles cause the magnetic field distortion; 4) current injection generates additional losses; 5) pole-slot matching limits the flexibility of the motor applications. Therefore, the development of cogging torque suppression methods with fewer undesirable effects is crucial and warrants further research.

In this paper, a new method for cogging torque suppression based on flux harmonic configuration (FHC) is proposed. It aims to reduce the cogging torque of IPM machines by shaping the rotor core profile. A clear and effective methodological path,

Shuangxia Niu, Litao Dai and W.L. Chan are with the Hong Kong Polytechnic University, Hong Kong, 999077, China (e-mail: eesxniu@polyu.edu.hk; email: litao.dai@polyu.edu.hk; wai-lok.chan@polyu.edu.hk; corresponding author: Shuangxia Niu).

Jian Gao, Kun Liu, and Shoudao Huang are with the Hunan University, Changsha, 410082, China (email: gaojian0895@hnu.edu.cn; kunliu@hnu.edu.cn; hsd1962@hnu.edu.cn).

based on the principle of harmonic interaction, is presented and validated through extensive case studies. The contributions of this paper can be summarized as follows:

1) This paper presents a clear optimization path to achieve significant suppression of cogging torque by changing only a few structural parameters.
2) The proposed method causes less degradation of other important electromagnetic properties of PM machines, while effectively reducing overall torque ripple.
3) The method can be extended to other machine structures troubled by cogging torque, such as axial-flux PM machines and PM linear machines.

The paper is organized as follows: Section II develops the cogging torque model based on the harmonic interaction. In Section III, the implementation of the proposed FHC method is elaborated. Section IV presents a comprehensive investigation of several motor case studies with different topologies. Additionally, Section V evaluates the effectiveness of the proposed method through simulations and experiments. Finally, Section VI concludes the paper.

II. Harmonic Model of Cogging Torque

Cogging torque arises from the interaction between rotor flux harmonics and uneven airgap magnetic reluctance harmonics caused by slotting. Therefore, to accurately analyze the cogging torque characteristics, it is essential to investigate the harmonic components of both the rotor flux and airgap reluctance.

A. Harmonic Forms of PMSMs

In the presence of motor manufacturing imperfections and unique structural designs, cogging torque can exhibit irregular harmonic patterns, including low-order harmonics associated with the mechanical cycle and an amplified magnitude [22]. To establish a standardized model and streamline the analysis of cogging torque, the following assumptions are proposed:

1) Rotor flux harmonics only include odd-order harmonics corresponding to the electrical period, disregarding even-order harmonics or mechanical period harmonics caused by uneven magnetization of the PMs, asymmetric pole shaping, or rotor eccentricity.
2) The period of airgap reluctance harmonics is defined as the distance between adjacent tooth centers, disregarding mechanical period harmonics resulting from asymmetrical tooth design or manufacturing imperfections.

For regular structures with symmetric magnetic poles, the rotor MMF can be expanded in Fourier form as

$$F_r(\theta_m,t)=\sum_{\nu_r}^{\infty}(-1)^{\frac{\nu_r-1}{2}}A_{Fr}(\nu_r)\cos(\nu_r p_N(\theta_m-\omega_m t)) \quad (1)$$

where ν_r is the harmonic order of the rotor MMF with $\nu_r=1,3,\dots,(2n+1)$. A_{Fr} is the amplitude of the ν_rth rotor MMF harmonic, p_N is the number of pole-pairs, θ_m is the mechanical angle, ω_m is the mechanical speed, and t is the running time.

Furthermore, the slotting causes non-uniformity of the airgap reluctance along the circumference, which can be represented in the following spatial harmonic form

$$\Lambda_{\mathrm{s}}(\theta_m)=\sum_{\nu_{\mathrm{Z}}}^{\infty}\Lambda_{\mathrm{As}}(\nu_{\mathrm{Z}})\cos(\nu_{\mathrm{Z}}Z_1\theta_m) \quad (2)$$

where ν_{Z} is the slot harmonic order, for symmetrical slot structures with $\nu_{\mathrm{Z}}=0,1,2,\dots,n$. Λ_{As} is the amplitude of ν_{Z}th slot harmonic, Z_1 is the number of slots.

Therefore, according to (1) and (2), the unified expression for the air-gap flux density with slotting effect is as follows

$$\begin{aligned}B_{\delta\mathrm{H}}(\theta_m,t)&=F_r(\theta_m,t)\Lambda_{\mathrm{s}}(\theta_m)/S_\delta\\&=\sum_{\nu_r}^{\infty}\sum_{\nu_{\mathrm{Z}}}^{\infty}\frac{(-1)^{\frac{\nu_r-1}{2}}}{2S_\delta}A_{Fr}(\nu_r)\Lambda_{\mathrm{As}}(\nu_{\mathrm{Z}})\big[\cos\big((\nu_r p_N-\nu_{\mathrm{Z}}Z_1)\theta_m\\&-\nu_r p_N\omega_m t\big)+\cos\big((\nu_r p_N+\nu_{\mathrm{Z}}Z_1)\theta_m-\nu_r p_N\omega_m t\big)\big]\end{aligned} \quad (3)$$

where S_δ is the active area of the air-gap.

B. Harmonic Model of Cogging Torque

The cogging torque can be accurately calculated using the energy method. Under no-load conditions, the magnetic energy in the airgap is given by

$$W_{\delta\mathrm{Mag}}=\int\frac{B_{\delta\mathrm{H}}(\theta_m,t)^2}{2\mu_0}dV_\delta \quad (4)$$

where μ_0 is the vacuum permeability, V_δ is the active volume of the airgap.

Next, the cogging torque can be calculated by

$$T_{\mathrm{cog}}=-\frac{\partial W_{\delta\mathrm{Mag}}}{\partial\omega_m t} \quad (5)$$

where its simplified expression of cogging torque is given by

$$\begin{aligned}T_{\mathrm{cog}}=K_C\sum_{\nu_{\mathrm{r1}}}^{+\infty}\sum_{\nu_{\mathrm{r2}}}^{+\infty}\sum_{\nu_{\mathrm{Z1}}}^{+\infty}\sum_{\nu_{\mathrm{Z2}}}^{+\infty}(-1)^{\left(\frac{\nu_{r1}+\nu_{r2}}{2}\right)}*\\A_{Fr}(\nu_{r1})A_{Fr}(\nu_{r2})\Lambda_{\mathrm{As}}(\nu_{\mathrm{Z1}})\Lambda_{\mathrm{As}}(\nu_{\mathrm{Z2}})\sin(\omega_{\mathrm{c}}t)\end{aligned} \quad (6)$$

where K_C is a coefficient related to the motor dimensions; ν_{r1} and ν_{r2} are the order of the rotor MMF harmonics; ν_{Z1} and ν_{Z2} are the order of the slot harmonics; ω_{c} is the number of cogging torques, subject to the following constraints

$$\omega_{\mathrm{c}}\in\mathrm{CM}\big((\nu_{r1}\pm\nu_{r2})p_N,(\nu_{\mathrm{Z1}}\pm\nu_{\mathrm{Z2}})Z_1\big)*\omega_m \quad (7)$$

where CM is the function of common multiple.

In summary, the cogging torque is determined by the specific combinations of the rotor MMF and slot harmonics. Fortunately, cogging torques of the same order generated by different harmonic combinations only differ in amplitude, while their phase angles are either the same or opposite.

Taking the widely used three-phase PM machine as an example, the cogging torque can be expressed in the following periodic form

$$T_{\mathrm{cog}}=\sum_{\nu_{\mathrm{cg}}=6,12,\dots,6n}^{+\infty}T_{\mathrm{cgH}}(\nu_{\mathrm{cg}})\sin(\nu_{\mathrm{cg}}p_N\omega_m t) \quad (8)$$

where ν_{cg} is the order of cogging torque, $\nu_{\mathrm{cg}}=6,12,\dots,6n$,

T_{cgH} is the amplitude of the ν_{cg}th cogging torque.

C. Relation Between Flux Harmonic and Cogging Torque

To illustrate the relationship between rotor MMF harmonics, slot harmonics, and cogging torque orders, TABLE I provides the typical combinations of effective cogging torque for three-phase PM machines. Notably, it is evident that multiple combinations of rotor MMF harmonics can generate cogging torque with the same order, and the resulting cogging torque may exhibit either positive or negative values depending on the specific MMF combinations employed.

TABLE I
ILLUSTRATION OF COGGING TORQUE HARMONIC LAWS

Order of cogging torque	Combination of rotor MMF harmonics	Combination of slot harmonics (If exists)	Initial phase
$\nu_{\mathrm{cg}}=6$	$(\nu_{r1},\nu_{r2})=(1,5)$	$(\nu_{Z1}\pm\nu_{Z2})=6p_N/Z_1$	180 deg
	$(\nu_{r1},\nu_{r2})=(1,7)$		0 deg
	$(\nu_{r1},\nu_{r2})=(3,3)$		180 deg
	$(\nu_{r1},\nu_{r2})=(3,9)$		0 deg
	...		
$\nu_{\mathrm{cg}}=12$	$(\nu_{r1},\nu_{r2})=(1,11)$	$(\nu_{Z1}\pm\nu_{Z2})=12p_N/Z_1$	0 deg
	$(\nu_{r1},\nu_{r2})=(1,13)$		180 deg
	$(\nu_{r1},\nu_{r2})=(3,9)$		0 deg
	$(\nu_{r1},\nu_{r2})=(5,7)$		0 deg
	...		
$\nu_{\mathrm{cg}}=18$	$(\nu_{r1},\nu_{r2})=(1,17)$	$(\nu_{Z1}\pm\nu_{Z2})=18p_N/Z_1$	180 deg
	$(\nu_{r1},\nu_{r2})=(1,19)$		0 deg
	$(\nu_{r1},\nu_{r2})=(3,15)$		180 deg
	...		
...			

More specifically, taking the 6th cogging torque ($T_{\mathrm{cog}}(6)$) exhibited by a 4-pole, 12-slot motor as an example, according to (6), (7) and TABLE I, it mainly originates from three cogging torque components of the same frequency, as shown below:

$$\begin{cases} T_{\mathrm{cog}}(6)\approx T_{\mathrm{cog.1}}+T_{\mathrm{cog.2}}+T_{\mathrm{cog.3}} \\ T_{\mathrm{cog.1}}=-K_C A_{Fr}(1)A_{Fr}(5)\Lambda_{\mathrm{As0}}\Lambda_{\mathrm{As1}}\sin(6p_N\omega_m t) \\ T_{\mathrm{cog.2}}=K_C A_{Fr}(1)A_{Fr}(7)\Lambda_{\mathrm{As0}}\Lambda_{\mathrm{As1}}\sin(6p_N\omega_m t) \\ T_{\mathrm{cog.3}}=-K_C A_{Fr}(3)A_{Fr}(3)\Lambda_{\mathrm{As0}}\Lambda_{\mathrm{As1}}\sin(6p_N\omega_m t) \end{cases} \tag{9}$$

where Λ_{As0}, Λ_{As1} represent the 0th and 1st harmonics of the airgap reluctance, respectively. It can be observed that the 6th cogging torque is influenced by the 3rd, 5th, and 7th harmonics of the rotor MMF flux. Therefore, in theory, modifying any of these harmonics can alter the existing cogging torque, either increasing or decreasing it.

III. FHC-BASED COGGING TORQUE SUPPRESSION

Based on the conclusion that changing rotor MMF harmonics can reduce cogging torque, this section provides a detailed description of the method to construct the rotor reluctance by altering the rotor surface shape to achieve the desired flux harmonics.

A. Principle of FHC

The rotor reluctance can be expressed as a general harmonic form of magnetic conductance as follows

$$\begin{aligned} &K_{\mathrm{sr}}(\theta_m,t) \\ &=K_{\mathrm{A0}}+(-1)^{\frac{\nu_{\mathrm{sr}}-1}{2}}K_{\mathrm{AH}}(\nu_{\mathrm{sr}})\cos\left(\nu_{\mathrm{sr}}p_N(\theta_m-\omega_m t)\right) \end{aligned} \tag{10}$$

where K_{A0} is the constant component, ν_{sr} is the conductance harmonic, and K_{AH} is the amplitude of the ν_{sr}th harmonic.

Since the fundamental component of the rotor MMF is the most significant, the rotor reluctance harmonic primarily interacts with it, resulting in changes in flux harmonics. By combining (1) and (10), their interactions are as follows

$$\begin{aligned} F_{\mathrm{sr}}(\theta_m,t)&=F_{r(\nu_r=1)}(\theta_m,t)K_{\mathrm{sr}}(\theta_m,t) \\ &=A_{Fr1}K_{\mathrm{A0}}\cos\left(p_N(\theta_m-\omega_m t)\right)+ \\ &(-1)^{\frac{\nu_{\mathrm{sr}}-1}{2}}\frac{A_{Fr1}K_{\mathrm{AH}}(\nu_{\mathrm{sr}})}{2}\cos((\nu_{\mathrm{sr}}\pm1)p_N(\theta_m-\omega_m t)) \end{aligned} \tag{11}$$

where A_{Fr1} is the fundamental component of the rotor MMF.

In summary, the rotor reluctance with a specific harmonic (ν_{sr}) interacts with the fundamental rotor MMF, generating two forms of flux harmonics, i.e., the ($\nu_{\mathrm{sr}}\pm1$)th flux harmonics. Fig. 1 illustrates the harmonic interaction between the 4th rotor reluctance harmonic and the fundamental rotor MMF.

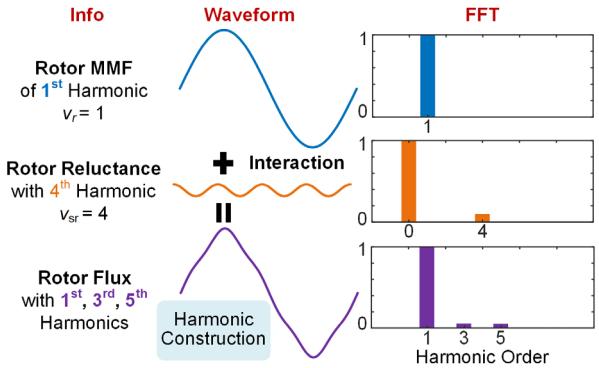

Fig. 1. Illustration of the proposed FHC method.

B. Reluctance Construction Method

This paper presents an approach to configure rotor reluctance harmonics by altering the surface of the rotor core to achieve a sinusoidal shape. The rotor core profile is defined by the following function:

$$\begin{cases} X(\theta_m)=\left[R_{\mathrm{r1c}}+\sum_{\nu_{\mathrm{sr}}}R_H(\nu_{\mathrm{sr}})\cos(\nu_{\mathrm{sr}}p_N\theta_m)\right]\cos(\theta_m) \\ Y(\theta_m)=\left[R_{\mathrm{r1c}}+\sum_{\nu_{\mathrm{sr}}}R_H(\nu_{\mathrm{sr}})\cos(\nu_{\mathrm{sr}}p_N\theta_m)\right]\sin(\theta_m) \end{cases} \tag{12}$$

where X and Y represent Cartesian coordinates corresponding to the mechanical circumferential angle ($\theta_m\in[0,2\pi]$), R_{r1c} denotes the radius of the center line of the sinusoidal curve, and R_H represents the amplitude of the sinusoidal curve.

Fig. 2 shows the schematic of constructing different reluctance harmonics by modifying the rotor core profile. It illustrates that by constructing even-order reluctance harmonics (ν_{sr}), the ($\nu_{\mathrm{sr}}\pm1$)th flux harmonics can be generated.

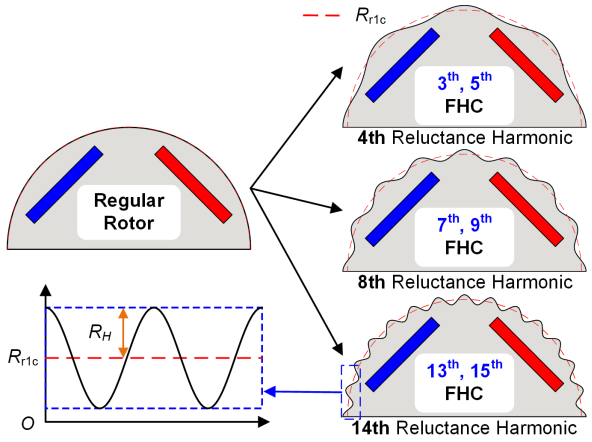

Fig. 2. Diagram of reluctance construction by changing the rotor profile.

C. Design Process

This section presents the design process of the proposed method and provides design considerations for its application. The flowchart, depicted in Fig. 3, illustrates the detailed steps for optimizing the cogging torque, which include:

1) Preliminary research to determine the cogging torque order of the initial motor.
2) Harmonic analysis to identify the rotor MMF orders that influence the cogging torque.
3) Selection of an optimal FHC path to construct the specific order of reluctance harmonic.
4) Parameter scanning for the selected reluctance harmonic.

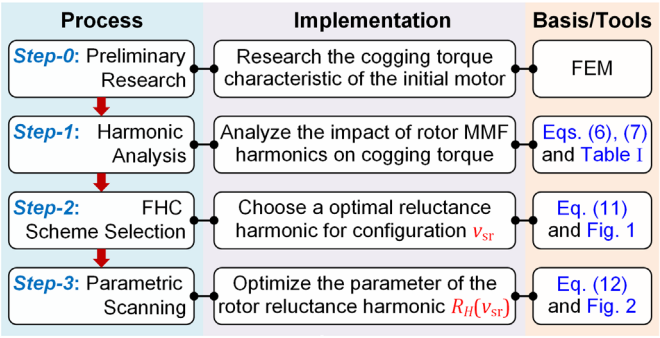

Fig. 3. Design process for FHC-based cogging torque suppression.

Furthermore, it is crucial to consider the following factors when determining the parameter scan range in Step-3 of the flowchart: 1) The optimal reluctance parameter, R_H, is typically smaller than the airgap thickness to prevent a significant decrease in torque; 2) Higher-order FHC requires a narrower search range as configuring higher-order fluxes is more effective; 3) The cogging torque exhibits a distinct single-valley characteristic, which allows for the determination of positive and negative intervals for the optimal reluctance parameter around its zero-crossing point.

D. Discussion on Additional Effects of the FHC Method

A desirable design method should not only help suppress cogging torque but also consider overall motor performance. Thereby, this section investigates the additional effects of the proposed FHC method through theoretical analysis.

1) *Influence on Average Torque*

The influence on average torque stems from the increase in effective airgap volume caused by the FHC. Assuming that the maximum rotor outer diameter remains the same for both the initial design and the FHC design, and the rotor leakage remains unchanged before and after modifying the rotor surface, the torque loss can be calculated as follows:

$$T_{\mathrm{D}} = \frac{R_H}{\delta + R_H} \tag{13}$$

where δ represents the airgap thickness of the initial design. Therefore, a smaller value of R_H is preferred.

2) *Influence on Torque Ripple*

The torque ripple in IPMSMs originates from the interaction of field harmonics and can be expressed as follows:

$$T_r = T_{\mathrm{cog}} + T_{rs}(F_{rH}, F_{sH}) + T_{rr}(F_{rH}, \Lambda_{rH}) \tag{14}$$

where T_{rs} and T_{rr} represent the ripple in synchronous torque and reluctance torque, respectively. F_{rH}, F_{sH}, and Λ_{rH} denote the rotor flux harmonics, stator MMF harmonics, rotor reluctance harmonics, respectively.

Although modifying the reluctance harmonics may affect the ripple in synchronous torque and reluctance torque, effectively suppressing cogging torque is typically beneficial in reducing overall torque ripple as cogging torque is the most prominent ripple in PMSMs.

3) *Influence on Electromotive Force (EMF) Distortion*

The v_{sr}-th reluctance harmonic modulates the $(v_r \pm 1)$-th flux harmonics, resulting in corresponding changes in the back-EMF. However, in cases where $(v_r \pm 1)$ is a multiple of 3, cancellation occurs due to the star connection of the windings. The remaining k-th harmonics are further reduced by the winding pitch and distribution factors defined as follows:

$$k_p(k) = \sin\left(\frac{k\theta_{ws}}{2}\right), k_d(k) = \frac{\sin\left(\frac{qk\alpha}{2}\right)}{\sin\left(\frac{k\alpha}{2}\right)} \tag{15}$$

where θ_{ws} represents the coil pitch angle, q is the wingding distribution number, and α is the electrical angle between the distributed windings.

Consequently, the resulting EMF may be either increased or decreased, depending on the amplitude and direction of the initial flux harmonics and modulated reluctance harmonics.

4) *Influence on Power Factor*

Due to the fact that reluctance harmonic modulation does not change the phase of the flux fundamental, it is theoretically expected not to cause phase shift in the airgap working fluxes, and thus not result in changes to the power factor.

IV. Case Studies

To validate the efficacy and versatility of the proposed method, three case studies were conducted on PM machines with different IPM rotor types and pole-slot combinations, and consequential different orders of cogging torque.

The main structural parameters were kept uniform to facilitate a meaningful comparison of the different solutions. These unified parameters are presented in TABLE II.

TABLE II
UNIFIED PARAMETERS OF CASE STUDIES

Parameter	Value	Parameter	Value
Stator outer diameter	130 mm	Stator inner diameter	75 mm
Ratio of slot opening	0.31	Air-gap thickness	1 mm
Ratio of slot depth	0.62	Tooth tip thickness	4 mm
Ratio of tooth width	0.40	Motor length	60 mm

A. Case Study I: 4P12S Horizontal IPM Machine

According to the implementation process illustrated in Fig. 3, it is essential to investigate the dominant cogging torque order before performing FHC. In this case, the relevant information is presented in TABLE III. The table indicates that the 6th cogging torque is primarily influenced by three specific flux harmonics ($\nu_r = 3, 5, 7$), as indicated in TABLE I. Furthermore, the corresponding reluctance harmonics ($\nu_{sr} = 2, 4, 8$) can modulate these three flux harmonics accordingly, while the reluctance harmonic ($\nu_{sr} = 6$) can simultaneously modulate the adjacent flux harmonics ($\nu_r = 5, 7$). Consequently, these specific reluctance harmonics are selected as optimizing parameters to suppress cogging torque.

To clearly demonstrate the impact of parameter variations on cogging torque, parametric scans are conducted for the four FHC schemes. It is noteworthy that in these scanning processes, only one parameter, i.e., the amplitude of rotor reluctance harmonic $R_H(\nu_{\mathrm{sr}})$, needs to be modified for each process. The results of FHC optimization are illustrated in Fig. 4, showcasing the scanning variations, waveform comparisons of cogging torque, and electromagnetic torque (at a current density of $3\mathrm{A/mm}^2$) between the initial scheme and the selected FHC schemes, as well as the optimized FHC structures. From Fig. 4, it is evident that all FHC approaches exhibit a significant suppressing effect on cogging torque, with small changes in the amplitude of reluctance harmonics

TABLE III
DOMINANT COGGING TORQUE AND ITS INFLUENCES OF CASE I

Dominant cogging torque	Noteworthy flux harmonics	Flux harmonic to be configured	Modulated reluctance order
$\nu_{\mathrm{cg}} = 6$	$(\nu_{r1}, \nu_{r2}) = (1, 5)$	$\nu_r = 5$	$\nu_{\mathrm{sr}} = 4$
	$(\nu_{r1}, \nu_{r2}) = (1, 7)$	$\nu_r = 7$	$\nu_{\mathrm{sr}} = 8$
	$(\nu_{r1}, \nu_{r2}) = (1, 5)$ and $(\nu_{r1}, \nu_{r2}) = (1, 7)$	$\nu_r = 5, 7$	$\nu_{\mathrm{sr}} = 6$
	$(\nu_{r1}, \nu_{r2}) = (3, 3)$	$\nu_r = 3$	$\nu_{\mathrm{sr}} = 2$

Moreover, it is crucial to evaluate other key performance indicators of the motor, including average torque ($I_{rms} = 3\mathrm{A/mm}^2$), torque ripple (peak-to-peak to average ratio), total harmonic distortion (THD) of phase-to-phase back-EMF, and power factor. These indicators collectively determine the effectiveness of the proposed approach in this paper. The comprehensive evaluation results are summarized in TABLE IV. The comparison of these indicators reveals that the 3rd FHC in this case exhibits the best overall performance. Specifically, it achieves a remarkable 67.4% suppression of cogging torque, a 57.7% reduction in torque ripple, and a 55.0% reduction in THD of line back-EMF.

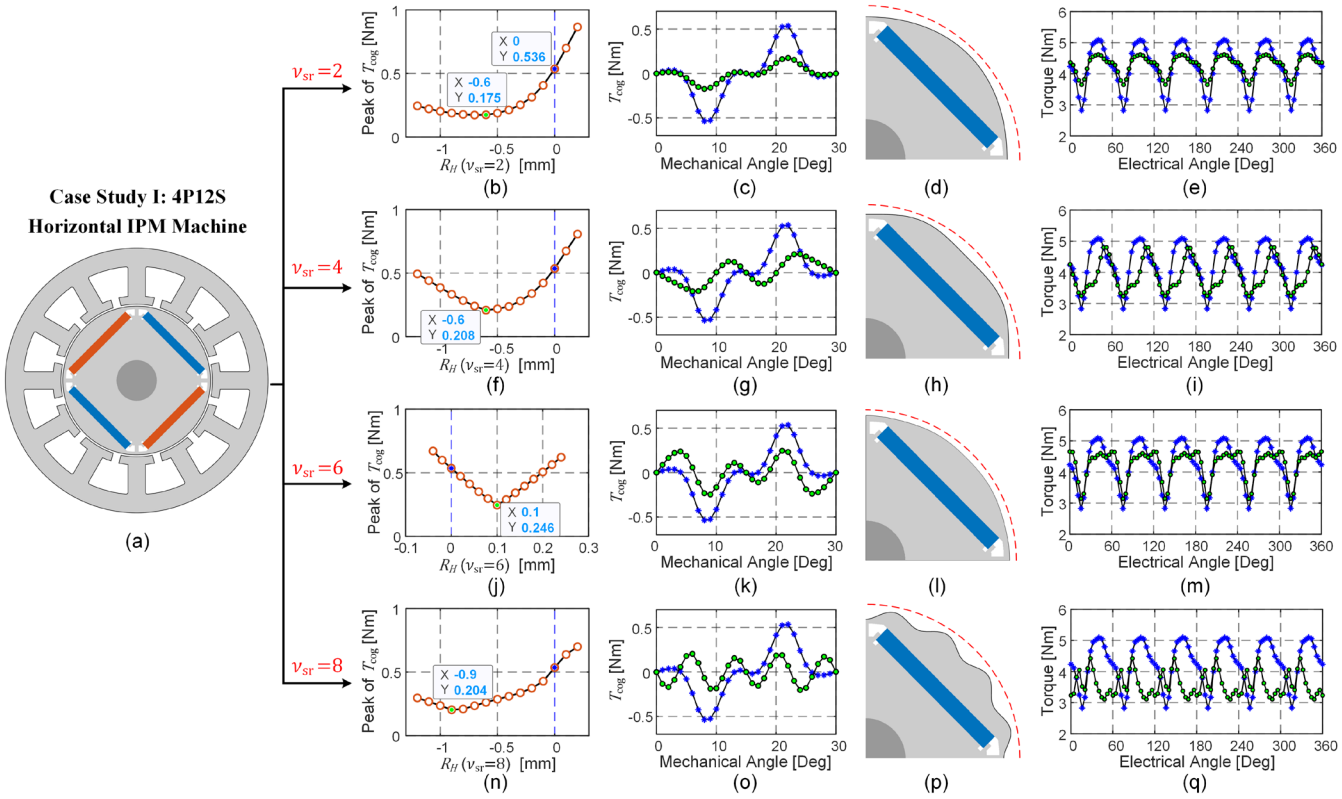

Fig. 4. Study of Case I. (a) represents the initial motor structure; (b), (f), (j), (n) depict parameterized scans for different cases; (c), (g), (k), (o) show waveform comparisons of cogging torque between the selected FHC schemes and the initial scheme; (d), (h), (l), (p) illustrate structural details of the selected FHC schemes; (e), (i), (m), (q) display waveform comparisons of electromagnetic torque at current density of 3A/mm^2.

TABLE IV
COMPREHENSIVE PERFORMANCE COMPARISON OF CASE I

Scheme	Peak of T_{cog} (Nm)	Average torque (Nm)	Torque ripple (%)	THD of EMF (%)	Power factor
Initial design	0.536	4.25	53.41	11.1	0.93
3rd FHC ($v_{sr}=2$)	0.175	4.28	22.61	5.0	0.96
5th FHC ($v_{sr}=4$)	0.208	3.92	39.99	23.6	0.94
5th and 7th FHC ($v_{sr}=6$)	0.246	4.24	36.63	14.7	0.93
7th FHC ($v_{sr}=8$)	0.204	3.58	36.74	23.8	0.94

B. Case Study II: 4P18S Double-I IPM Machine

In this case study, a fractional-slot structure with 4 poles and 18 slots was investigated. Due to the relatively large least common multiple of the pole and slot numbers, the cogging torque exhibits a relatively high frequency, and its magnitude is not pronounced. The dominant order of the cogging torque and the combination of flux harmonics influencing it can be found in TABLE V. It can be observed that, theoretically, the cogging torque can be suppressed in this structure by constructing the 16th, 20th, 18th, and 2nd harmonics of rotor reluctance.

Similar to Case-I, parametric scans are performed on the four FHC approaches in this case. The optimization results are shown in Fig. 5. It can be observed that the structural modifications in this case are minimal, owing to the relatively small magnitude of the high-order flux harmonics. Specifically, in the high-order FHC approaches, the optimized parameters of $R_H(16)$, $R_H(20)$, and $R_H(18)$ are only -0.08mm, -0.03mm, and 0.02mm, respectively. This indicates that their impact on average torque loss is minimal. However, their effectiveness in reducing cogging torque is significantly pronounced.

TABLE V
DOMINANT COGGING TORQUE AND ITS INFLUENCES OF CASE II

Dominant cogging torque	Noteworthy flux harmonics	Flux harmonic to be configured	Modulated reluctance order
$v_{cg}=18$	$(v_{r1},v_{r2})=(1,17)$	$v_r=17$	$v_{sr}=16$
	$(v_{r1},v_{r2})=(1,19)$	$v_r=19$	$v_{sr}=20$
	$(v_{r1},v_{r2})=(1,17)$ and $(v_{r1},v_{r2})=(1,19)$	$v_r=17,19$	$v_{sr}=18$
	$(v_{r1},v_{r2})=(3,15)$	$v_r=3$	$v_{sr}=2$

The overall performances of the optimal FHC schemes and the initial scheme are comprehensively compared and summarized in TABLE VI.

TABLE VI
COMPREHENSIVE PERFORMANCE COMPARISON OF CASE II

Scheme	Peak of T_{cog} (Nm)	Average torque (Nm)	Torque ripple (%)	THD of EMF (%)	Power factor
Initial design	0.128	4.06	10.7	3.01	0.93
17th FHC ($v_{sr}=16$)	0.024	4.05	17.28	6.01	0.93
19th FHC ($v_{sr}=20$)	0.034	4.06	8.81	2.40	0.93
17th and 19th FHC ($v_{sr}=18$)	0.026	4.06	13.26	3.39	0.93
3rd FHC ($v_{sr}=2$)	0.002	3.84	1.75	2.26	0.97

The results of the comparison indicate that the 19th FHC design demonstrates excellent overall performance, achieving a remarkable 73.4% reduction in cogging torque and a 17.7%

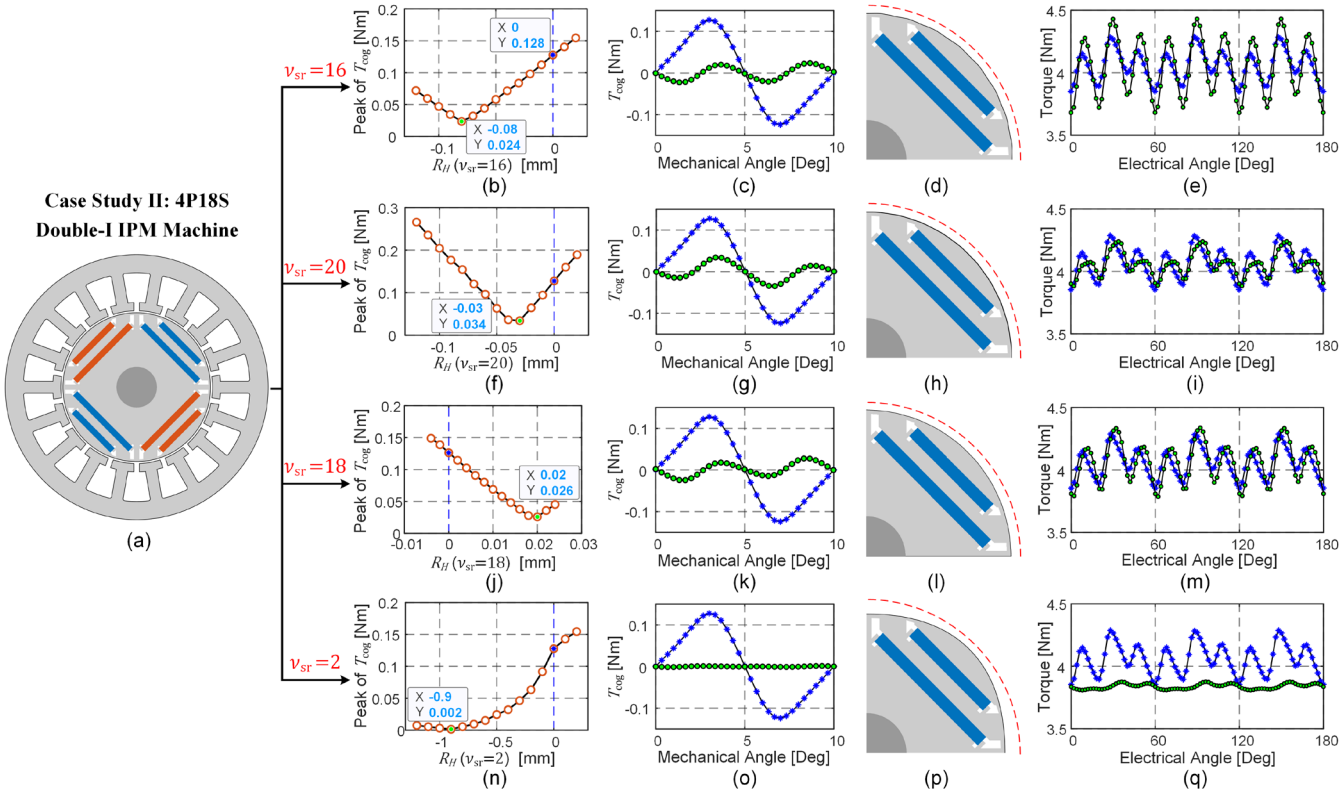

Fig. 5. Study of Case II. (a) represents the initial motor structure; (b), (f), (j), (n) depict parameterized scans for different cases; (c), (g), (k), (o) show waveform comparisons of cogging torque between the selected FHC schemes and the initial scheme; (d), (h), (l), (p) illustrate structural details of the selected FHC schemes; (e), (i), (m), (q) display waveform comparisons of electromagnetic torque at current density of 3A/mm^2.

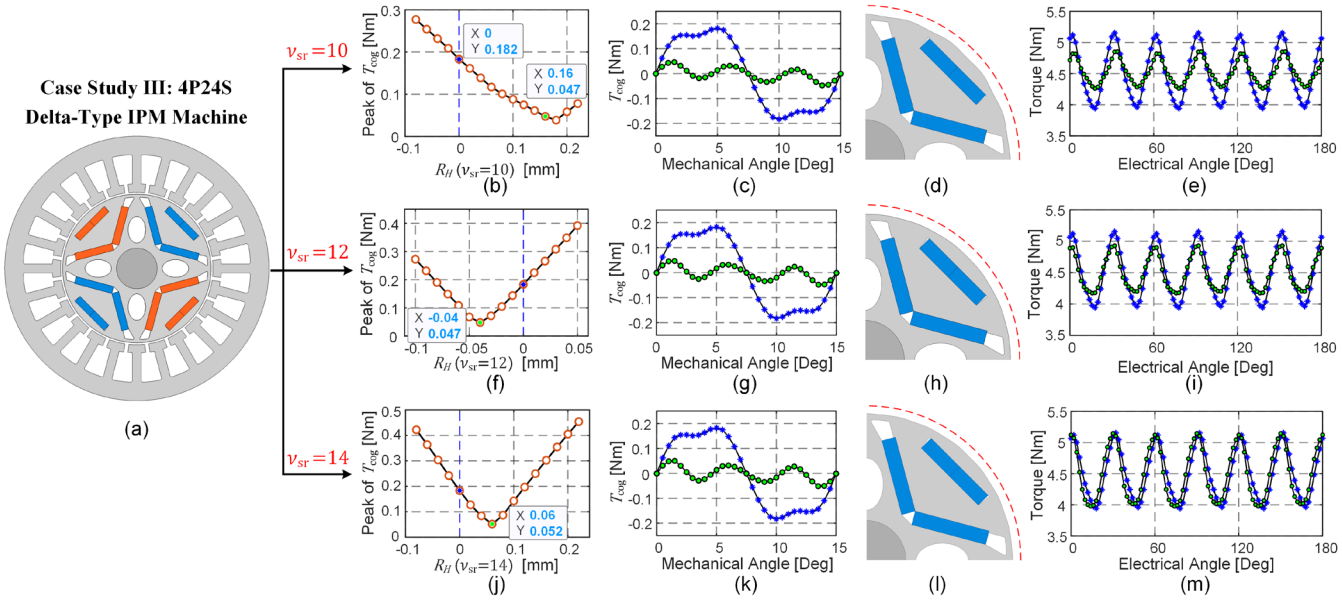

Fig. 6. Study of Case III. (a) represents the initial motor structure; (b), (f), (j) depict parameterized scans for different cases; (c), (g), (k) show waveform comparisons of cogging torque between the selected FHC schemes and the initial scheme; (d), (h), (l) illustrate structural details of the selected FHC schemes; (e), (i), (m) display waveform comparisons of electromagnetic torque at current density of 3A/mm^2.

decrease in torque ripple. Additionally, it is worth noting that the 3rd FHC design exhibits the best suppression effects on both cogging torque and torque ripple. However, it is important to consider that the average torque is reduced due to the reduced width of the PMs.

C. Case Study III: 4p24s Delta-Type IPM Machine

The final case examines a typical pole-slot combination commonly employed in electric vehicle applications, such as 8p48s and 6p36s motors. In this scenario, the lowest order of cogging torque is the 12th harmonic, which is also the most significant, as indicated in TABLE VII.

TABLE VII
DOMINANT COGGING TORQUE AND ITS INFLUENCES OF CASE III

Dominant cogging torque	Noteworthy flux harmonics	Flux harmonic to be configured	Modulated reluctance
$\nu_{cg}=12$	$(\nu_{r1},\nu_{r2})=(1,11)$	$\nu_r=11$	$\nu_{sr}=10$
	$(\nu_{r1},\nu_{r2})=(1,11)$ and $(\nu_{r1},\nu_{r2})=(1,13)$	$\nu_r=11,13$	$\nu_{sr}=12$
	$(\nu_{r1},\nu_{r2})=(1,13)$	$\nu_r=13$	$\nu_{sr}=14$

For the purpose of cogging torque suppression, the FHC approaches with reluctance harmonics $\nu_{sr}=10,12,14$ were chosen for this case study. The parametric scans and optimization results for cogging torque, rotor structure, and electromagnetic torque are presented in Fig. 6. Notably, all FHC approaches exhibit effective reduction of cogging torque while introducing minimal changes to the rotor surface. The optimized parameters for the three FHCs are as follows: $R_H(10)=0.16$ mm, $R_H(12)=-0.04$ mm, and $R_H(14)=0.06$ mm. A comprehensive evaluation of the overall performance for these optimized schemes is provided in TABLE VIII, highlighting that the 11th FHC achieves favorable overall performance. It demonstrates a remarkable 74.2% reduction in cogging torque, a significant 51.3% reduction in torque ripple, and an improvement in the THD of the back-EMF to some extent.

To validate the proposed method experimentally, motor prototypes were manufactured for both the optimized 11th FHC scheme and the initial scheme. The stator and rotor steel laminations of these prototypes are depicted in Fig. 7. Upon comparing the structures, it can be observed that the alterations made to the rotor surface are not substantial. This suggests that the effective airgap volume will not experience a significant increase, thereby avoiding a reduction in the output torque.

TABLE VIII
COMPREHENSIVE PERFORMANCE COMPARISON OF CASE III

Scheme	Peak of T_{cog} (Nm)	Average torque (Nm)	Torque ripple (%)	THD of EMF (%)	Power factor
Initial design	0.182	4.51	26.9	4.17	0.98
11th FHC ($\nu_{sr}=10$)	0.047	4.52	13.1	3.88	0.98
11th and 13th FHC ($\nu_{sr}=12$)	0.047	4.50	16.8	2.12	0.98
13th FHC ($\nu_{sr}=14$)	0.052	4.50	26.0	5.92	0.98

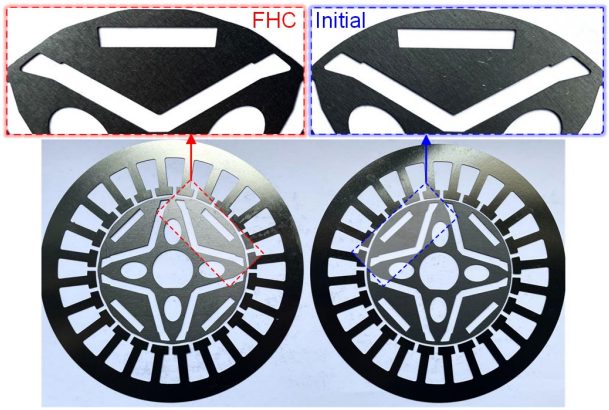

Fig. 7. Comparison of steel laminations between the 11th FHC scheme and the initial scheme of Case III.

V. Comprehensive Investigation and Validation

In general, the effects resulting from the cogging torque suppression method may be more significant than the cogging torque itself. These effects can include potential THD of the back-EMF, increased torque ripple, decreased average output torque, and so on. Therefore, it is essential to conduct a comprehensive investigation into these additional effects. In this section, Case III is thoroughly analyzed.

The experimental validation includes cogging torque testing and load torque testing. The prototypes and testing platforms are illustrated in Fig. 8. It is notable that cogging torque testing is conducted using weight measurement, while load torque testing is performed using torque transducer measurement.

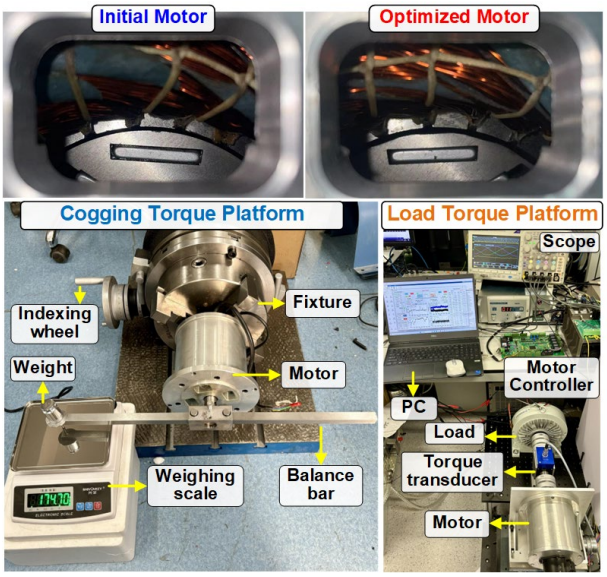

Fig. 8. Motor prototypes and testing platforms.

A. No-Load Performance Validation

Cogging torque tests were conducted on both the initial and optimized motors using a weight measuring platform, as shown in Fig. 8. The comparison of cogging torque between the initial and optimized motors, based on both simulated and tested results, is presented in Fig. 9.

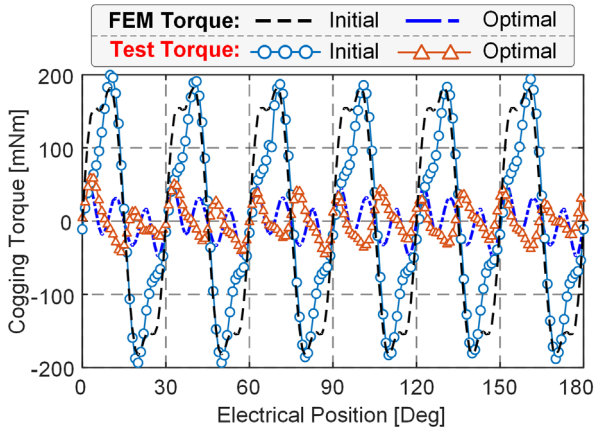

Fig. 9. Cogging torque comparison between simulation and test results.

The comparison indicates a close agreement in cogging torque magnitude between the FEM and test results. However, certain differences are observed in the higher-order cogging torque components, particularly in the optimized motor. Nevertheless, it is worth mentioning that the optimized motor exhibits a significant reduction in cogging torque.

The phase-phase back EMFs of the two motors were also tested to verify their manufacturing accuracy. Fig. 10 illustrates the comparison of the back EMF waveforms between FEM simulation and experimental results for both motors, with a controlled speed of 360 rpm. The comparison reveals a strong agreement between the simulated and measured values, thereby confirming the manufacturing accuracy of the motors.

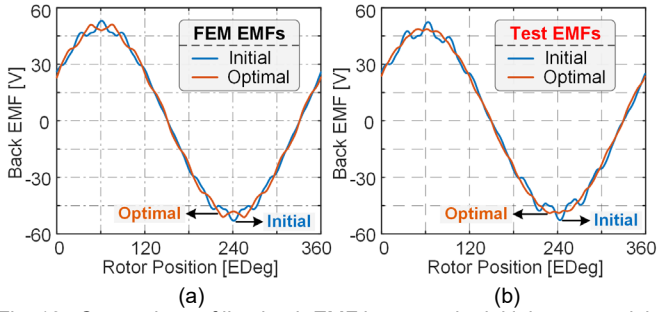

(a) (b)

Fig. 10. Comparison of line back-EMF between the initial motor and the optimal motor. (a) Simulation results. (b) Experimental results.

B. On-Load Performance Validation

In order to compare the rated load performance between the initial motor and the optimized motor, both motors were subjected to the same controller, control parameters, and load conditions. The experimental platform is shown in Fig. 8, and the measured three-phase currents and shaft torque for one mechanical cycle of both motors are presented in Fig. 11.

From the comparison, it can be observed that both motor current waveforms exhibit good sinusoidal characteristics, indicating minimal additional torque ripple caused by current harmonics. In terms of torque, the two motors demonstrate similar torque output capabilities, while the optimized motor exhibits noticeably reduced torque ripple compared to the initial motor.

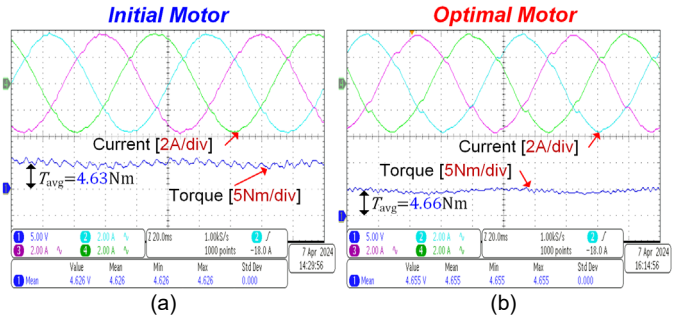

(a) (b)

Fig. 11. Measured currents and torque waveforms under load conditions. (a) Initial motor. (b) Optimal motor.

Moreover, the torque ripple of both the initial and optimized motors was analyzed using FEM simulation and experimental testing under load conditions corresponding to approximately 33%, 66%, and 100% of the rated load. The comparative simulation results are presented in Fig. 12, while the comparative experimental results are shown in Fig. 13. The figures clearly demonstrate the varying degrees of torque ripple suppression achieved by the proposed FHC design method

across different load conditions.

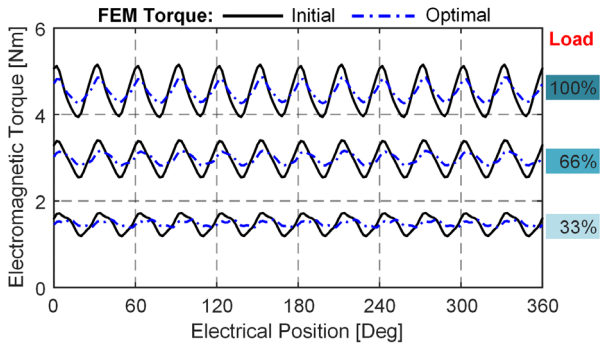

Fig. 12. Simulation torque comparison under different load conditions.

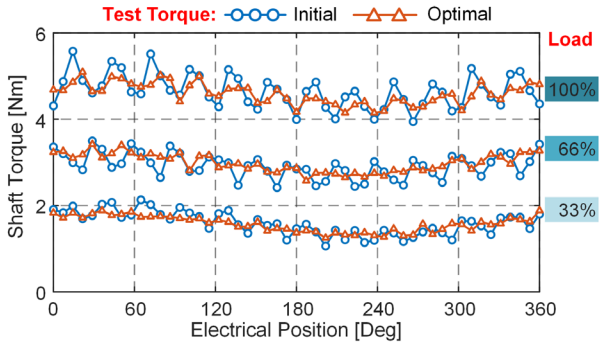

Fig. 13. Test torque comparison under different load conditions.

C. Tolerance Analysis on the Proposed Method

The effectiveness of cogging torque suppression in the presence of rotor manufacturing errors is investigated through Monte Carlo analysis in a fault-tolerant framework [23]. Each pole-pair's rotor surface is modeled using ten segmented curves, where each segment corresponds to a single-period cosine function. The amplitude of the cosine function is determined by the coefficient r_{Ci} $(i = 1, \dots, 10)$, with $r_{Ci} = 1$ indicating error-free manufacturing. To simulate manufacturing errors, the sampling process incorporates a variation range of 90% to 110% for each r_{Ci}, facilitating the determination of peak cogging torque values under diverse error parameter combinations. A schematic diagram depicting the variation of r_{Ci} $(i = 1, \dots, 10)$ within one pole pair range is shown in Fig. 14.

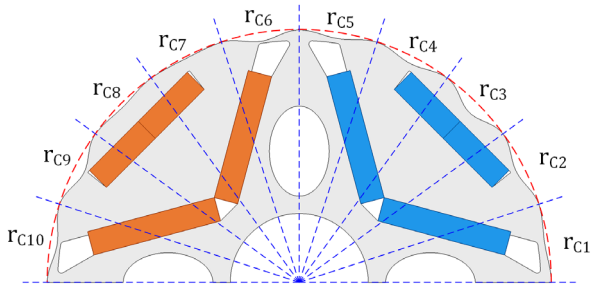

Fig. 14. Illustration depicting the variation of coefficients r_{Ci}.

The cogging torque response exhibits a normal distribution under parameter variations, as illustrated in Fig. 15. The normal distribution is characterized by a mean value of 47.121 mNm and a standard deviation of 6.093 mNm. The failure domain is defined as the region surpassing 150% of the mean value, which corresponds to approximately 70 mNm. Notably, the sigma level reaches 3.0137, resulting in a remarkably low failure probability of only 0.258%. This indicates that the proposed method demonstrates excellent robustness.

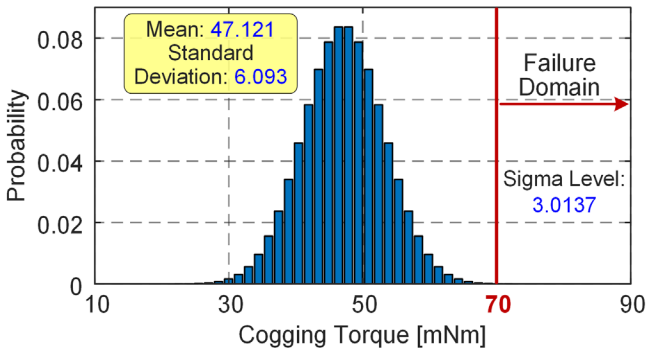

Fig. 15. Distribution of peak cogging torque under parameter variations.

VI. Conclusion

In this paper, a harmonic model of cogging torque in PMSMs is developed, revealing that the cogging torque can be suppressed by configuring the odd rotor flux harmonics through shaping the rotor profile to modulate the even rotor reluctance harmonics. In conclusion, the following conclusions can be drawn.

1) The proposed method has proven to be highly effective in suppressing cogging torque, as demonstrated through case studies involving various rotor structures and pole-slot combinations of PMSMs. Moreover, the tolerance analysis conducted on the proposed method highlights its excellent design tolerance capability.
2) The method is highly applicable and easy to implement since it only requires shaping the rotor profile. The paper presents different FHC paths as references, allowing for a rational selection that can effectively reduce cogging torque without compromising other crucial performances.
3) The proposed FHC method has good compatibility with other cogging torque suppression techniques, such as the skewed rotor and stator dummy slot methods. By combining these methods, it becomes possible to achieve further deep suppression of cogging torque.

References

[1] Z. Q. Zhu and D. Howe, "Influence of design parameters on cogging torque in permanent magnet machines," *IEEE Trans. Energy Convers.*, vol. 15, DOI: 10.1109/60.900501, no. 4, pp. 407-412, Dec. 2000.

[2] F. Ebadi, M. Mardaneh, A. Rahideh and N. Bianchi, "Analytical Energy-Based Approaches for Cogging Torque Calculation in Surface-Mounted PM Motors," *IEEE Trans. Magn.*, vol. 55, DOI: 10.1109/TMAG.2019.2906107, no. 5, pp. 1-10, May 2019.

[3] J. Wanjiku, M. A. Khan, P. S. Barendse and P. Pillay, "Influence of Slot Openings and Tooth Profile on Cogging Torque in Axial-Flux PM Machines," *IEEE Trans. Ind. Electron.*, vol. 62, DOI: 10.1109/TIE.2015.2458959, no. 12, pp. 7578-7589, Dec. 2015.

[4] Y. Guodong, Z. Jibin, X. Yongxiang, L. Yong, H. Jianhui and W. Qian, "Torque Performance Improvement of a Radial-Flux Slotted Limited-Angle Torque Motor by Tapered Tooth-Tip," *IEEE Trans. Appl. Supercond.*, vol. 26, DOI: 10.1109/TASC.2016.2594807, no. 7, pp. 1-5, Oct. 2016.

[5] Y. Yokoi and T. Higuchi, "Stator Design of Alternate Slot Winding for Reducing Torque Pulsation With Magnet Designs in Surface-Mounted Permanent Magnet Motors," *IEEE Trans. Magn.*, vol. 51, DOI: 10.1109/TMAG.2015.2394771, no. 6, pp. 1-11, June 2015.

[6] T. Liu, S. Huang, J. Gao and K. Lu, “Cogging Torque Reduction by Slot-Opening Shift for Permanent Magnet Machines,” *IEEE Trans. Magn.*, vol. 49, DOI: 10.1109/TMAG.2013.2239977, no. 7, pp. 4028-4031, July 2013.

[7] D. Wang, C. Peng, J. Li and C. Wang, “Comparison and Experimental Verification of Different Approaches to Suppress Torque Ripple and Vibrations of Interior Permanent Magnet Synchronous Motor for EV,” *IEEE Trans. Ind. Electron.*, vol. 70, DOI: 10.1109/TIE.2022.3156034, no. 3, pp. 2209-2220, March 2023.

[8] S. -G. Lee, S. Kim, J. -C. Park, M. -R. Park, T. H. Lee and M. -S. Lim, “Robust Design Optimization of SPMSM for Robotic Actuator Considering Assembly Imperfection of Segmented Stator Core,” *IEEE Trans. Energy Convers.*, vol. 35, DOI: 10.1109/TEC.2020.2999127, no. 4, pp. 2076-2085, Dec. 2020.

[9] V. Simón-Sempere, A. Simón-Gómez, M. Burgos-Payán and J. -R. Cerquides-Bueno, “Optimisation of Magnet Shape for Cogging Torque Reduction in Axial-Flux Permanent-Magnet Motors,” *IEEE Trans. Energy Convers.*, vol. 36, DOI: 10.1109/TEC.2021.3068174, no. 4, pp. 2825-2838, Dec. 2021.

[10] V. Simón-Sempere, M. Burgos-Payán and J. -R. Cerquides-Bueno, “Cogging Torque Cancellation by Magnet Shaping in Surface-Mounted Permanent-Magnet Motors,” *IEEE Trans. Magn.*, vol. 53, DOI: 10.1109/TMAG.2017.2676090, no. 7, pp. 1-7, July 2017.

[11] H. Mirahki, M. Moallem, M. Ebrahimi and B. Fahimi, “Asymmetrical Magnet Shape Optimization Based on S-C Mapping for Torque Profile Mitigation in Unidirectional Application of SPMS Machine,” *IEEE Trans. Transport. Electrific.*, vol. 5, DOI: 10.1109/TTE.2019.2928250, no. 3, pp. 630-637, Sept. 2019.

[12] W. Ren, Q. Xu, Q. Li and L. Zhou, “Reduction of Cogging Torque and Torque Ripple in Interior PM Machines With Asymmetrical V-Type Rotor Design,” *IEEE Trans. Magn.*, vol. 52, DOI: 10.1109/TMAG.2016.2530840, no. 7, pp. 1-5, July 2016.

[13] C. Peng, D. Wang, Z. Feng and B. Wang, “A New Segmented Rotor to Mitigate Torque Ripple and Electromagnetic Vibration of Interior Permanent Magnet Machine,” *IEEE Trans. Ind. Electron.*, vol. 69, DOI: 10.1109/TIE.2021.3063869, no. 2, pp. 1367-1377, Feb. 2022.

[14] D. Wang, X. Wang and S. -Y. Jung, “Cogging Torque Minimization and Torque Ripple Suppression in Surface-Mounted Permanent Magnet Synchronous Machines Using Different Magnet Widths,” *IEEE Trans. Magn.*, vol. 49, DOI: 10.1109/TMAG.2013.2242454, no. 5, pp. 2295-2298, May 2013.

[15] J. Gao, G. Wang, X. Liu, W. Zhang, S. Huang and H. Li, “Cogging Torque Reduction by Elementary-Cogging-Unit Shift for Permanent Magnet Machines,” *IEEE Trans. Magn.*, vol. 53, DOI: 10.1109/TMAG.2017.2712799, no. 11, pp. 1-5, Nov. 2017.

[16] M. Aydin and M. Gulec, “Reduction of Cogging Torque in Double-Rotor Axial-Flux Permanent-Magnet Disk Motors: A Review of Cost-Effective Magnet-Skewing Techniques With Experimental Verification,” *IEEE Trans. Ind. Electron.*, vol. 61, DOI: 10.1109/TIE.2013.2276777, no. 9, pp. 5025-5034, Sept. 2014.

[17] W. Fei and Z. Q. Zhu, “Comparison of Cogging Torque Reduction in Permanent Magnet Brushless Machines by Conventional and Herringbone Skewing Techniques,” *IEEE Trans. Energy Convers.*, vol. 28, DOI: 10.1109/TEC.2013.2270871, no. 3, pp. 664-674, Sept. 2013.

[18] P. Jalali, S. T. Boroujeni and J. Khoshtarash, “Expansion of the Feasible Slot/Pole Combinations in the Fractional Slot PM Machines by Applying Three-Slot Pitch Coils,” *IEEE Trans. Energy Convers.*, vol. 34, DOI: 10.1109/TEC.2018.2871889, no. 2, pp. 993-999, June 2019.

[19] H. Chen and C. H. T. Lee, “Parametric Sensitivity Analysis and Design Optimization of an Interior Permanent Magnet Synchronous Motor,” *IEEE Access*, vol. 7, DOI: 10.1109/ACCESS.2019.2950773, pp. 159918-159929, 2019.

[20] S. L. Ho, N. Chen and W. N. Fu, “An Optimal Design Method for the Minimization of Cogging Torques of a Permanent Magnet Motor Using FEM and Genetic Algorithm,” *IEEE Trans. Appl. Supercond.*, vol. 20, DOI: 10.1109/TASC.2009.2038717, no. 3, pp. 861-864, June 2010.

[21] J. Gao, Z. Xiang, L. Dai, S. Huang, D. Ni and C. Yao, “Cogging Torque Dynamic Reduction Based on Harmonic Torque Counteract,” *IEEE Trans. Magn.*, vol. 58, DOI: 10.1109/TMAG.2021.3093723, no. 2, pp. 1-5, Feb. 2022.

[22] J. Ou, Y. Liu, R. Qu, and M. Doppelbauer, “Experimental and Theoretical Research on Cogging Torque of PM Synchronous Motors Considering Manufacturing Tolerances,” *IEEE Trans. Ind. Electron.*, vol. 65, DOI: 10.1109/TIE.2017.2758760, no. 5, pp. 3772–3783, May 2018.

[23] L. Xu, W. Wu, W. Zhao, G. Liu and S. Niu, "Robust Design and Optimization for a Permanent Magnet Vernier Machine With Hybrid Stator," *IEEE Trans. Energy Convers.*, vol. 35, DOI: 10.1109/TEC.2020.3011925, no. 4, pp. 2086-2094, Dec. 2020.

Litao Dai (Member, IEEE) was born in Changsha, China, in 1993. He received the B.S. degree in mathematics from Harbin University of Commerce, Harbin, China, in 2015, and Ph.D. degree in electrical engineering from Hunan University, Changsha, China, in 2023.

He is currently working as a Postdoctoral Fellow with the Department of Electrical and Electronic Engineering, The Hong Kong Polytechnic University, Hong Kong, SAR, China.

Jian Gao received his B.E., M.E., and Ph.D. degrees in electrical engineering from Hunan University, Changsha, China, in 2001, 2004, and 2013, respectively.

From 2004 to 2021, he served as a Lecture and Associate Professor with the College of Electrical and Information Engineering, Hunan University, where he now served as a Full Professor. His research interests include high power/torque density motor design and control, wind energy conversion systems, and vehicle electric drive systems.

Shuangxia Niu (Senior Member, IEEE) received the B.Sc. and M.Sc. degrees from Tianjin University, Tianjin, China, in 2002 and 2005, and the Ph.D. degree from the University of Hong Kong, Hong Kong, SAR, China, in 2009, all in electrical engineering.

She is currently a professor with the Department of Electrical and Electronic Engineering, The Hong Kong Polytechnic University. She authored or coauthored more than 200 papers in leading journals. Prof. Niu is currently an Associate Editor for the IEEE Journal of Emerging and Selected Topics in Power Electronics.

Kun Liu was born in China, in 1998. He received the B.S. degree in electrical engineering from Anhui University of Science and Technology, Anhui, China, in 2020, and the M.E. degree in electrical engineering from Hunan University, Hunan, China, in 2023.

He is currently working as a research assistant with the College of Electrical and Information Engineering, Hunan University, Hunan, China.

Shoudao Huang (Senior Member, IEEE) received the B.S. and Ph.D. degrees in electrical engineering from Hunan University, Changsha, China, in 1983, and 2005, respectively.

He is currently a Full Professor with the College of Electrical and Information Engineering, Hunan University, China. His research interests include wind energy conversion system, generator design and control, and electronic system and control.

W. L. Chan (Senior Member, IEEE) received the B.Sc.(Eng.) and M.Phil. degrees from The University of Hong Kong, Hong Kong, in 1988 and 1993. He then received Ph.D. degree from City University London, London, U.K, in 2000.

He is now an Associate Professor in the Department of Electrical and Electronic Engineering, The Hong Kong Polytechnic University. Dr. Chan is the Vice Chairman of the International Association of Elevator Engineers (Hong Kong-China Branch).